CHALMERS
UNIVERSITY OF TECHNOLOGY

Aerodynamic drag improvements on a square-back vehicle at yaw using a tapered cavity and asymmetric flaps

Downloaded from: https://research.chalmers.se, 2024-07-27 08:40 UTC

Citation for the original published paper (version of record):
Urquhart, M., Varney, M., Sebben, S. et al (2020). Aerodynamic drag improvements on a square-back vehicle at yaw using a tapered cavity and asymmetric flaps. International Journal of Heat and Fluid Flow, 86(108737).
http://dx.doi.org/10.1016/j.ijheatfluidflow.2020.108737

N.B. When citing this work, cite the original published paper.

research.chalmers.se offers the possibility of retrieving research publications produced at Chalmers University of Technology.
It covers all kind of research output: articles, dissertations, conference papers, reports etc. since 2004.
research.chalmers.se is administrated and maintained by Chalmers Library

(article starts on next page)

International Journal of Heat and Fluid Flow 86 (2020) 108737

Contents lists available at ScienceDirect

International Journal of Heat and Fluid Flow

journal homepage: www.elsevier.com/locate/ijhff

Aerodynamic drag improvements on a square-back vehicle at yaw using a tapered cavity and asymmetric flaps

Magnus Urquhart [a,*], Max Varney [b], Simone Sebben [a], Martin Passmore [b]

[a] Chalmers University of Technology - Gothenburg, Sweden
[b] Loughborough University - Loughborough, England, United Kingdom

ARTICLE INFO

Keywords:
Aerodynamics
Tomographic PIV
Optimisation
Crossflow
Yaw
Drag
Wake

ABSTRACT

Emissions of greenhouse gasses from passenger vehicles is a concern globally. One of the factors that influence the vehicles energy consumption is the aerodynamic drag, continuing to be an active topic of interest. This work investigates the vehicle wake in relation to aerodynamic drag in steady crosswind conditions.

The vehicle used is a modified version of the generic Windsor geometry with wheels and a rearward-facing base cavity with nine angled surfaces, or flaps, distributed at the trailing edge of the cavity along the roof and sides. A surrogate model-based optimisation algorithm was used to minimise the drag coefficient by optimising the angle of each flap individually. The experiments were performed in the Loughborough University Large Wind Tunnel. The time-averaged and unsteady results of both the base pressures and tomographic Particle Image Velocimetry indicate that the optimised flap angles improve drag primarily by altering the wake balance. This is achieved by reducing the strength of a large leeward side vortex, reducing the crossflow within the wake.

1. Introduction

As global emissions become more of a concern, greenhouse gas and air quality regulations placed on passenger vehicles are becoming more stringent to meet emissions targets. For example, new European regulations impose punitive fines on manufacturers for exceeding fleet average CO_2 limits (European Parliament and Council of the European Union, 2014). As such, the need to improve total vehicle efficiency for both emissions reductions (internal combustion) and range extension (electric) is an ethical and financial necessity.

One way to improve the efficiency of a vehicle is by reducing the aerodynamic drag, which has a squared relationship with the vehicle velocity. This is particularly important as today's passenger vehicles travel at high velocities which is reflected in the latest driving cycle (World Harmonised Light vehicle Test Cycle [WLTC]) (Schuetz, 2015).

A popular vehicle shape in the passenger vehicle market is the Sports Utility Vehicle (SUV), accounting for 37.5% of new vehicles sold in Europe (JATO, 2019). SUVs are typically designed with limited tapering to the rear edges, for aesthetics, which results in a large region of low pressure in the separated wake and a reduction in pressure on the base. Therefore their aerodynamic drag tends to be higher than other vehicle types that are more tapered.

Applying a cavity to the base of the geometry, by extending plates from the base of the geometry, is one way to reduce the drag. When applied perpendicular to the base they are effective on simplified geometries at 0° yaw (Evrard et al., 2016; Duell and George, 1993; Bonnavion and Cadot, 2018), yielding up to an 11% drag reduction (Duell and George, 1993) through increasing the pressure at the rear of the geometry.

When cavities are applied to passenger vehicles or heavy goods vehicles, the cavity is typically tapered. Tapering, on its own, is an effective way of reducing the total and base drag (Howell et al., 2013; Ahmed et al., 1984; Varney et al., 2018a), but when implemented with a cavity, the drag reduction further improves (Cooper, 1985).

Another addition to cavity geometries has been a *kick* at the trailing edge of the cavity. This has previously been applied by Sterken et al. (2014) to the rear of a cavity along the sides and roof of an SUV. This was of benefit to the drag at all cavity lengths, particularly at yaw, with an additional reduction of $\approx 0.01C_D$ depending on the yaw angle and cavity depth. The additional drag reduction at yaw was later shown to correlate well, by Urquhart et al. (2018), with a reduction in wake crossflow and an increase in base pressure on the windward side.

Typically, aerodynamic modifications are assessed in idealised conditions. Low turbulence, 0° yaw and simplified geometries are useful

* Corresponding author.
E-mail addresses: magnus.urquhart@chalmers.se (M. Urquhart), m.varney@lboro.ac.uk (M. Varney), simone.sebben@chalmers.se (S. Sebben), m.a.passmore@lboro.ac.uk (M. Passmore).

https://doi.org/10.1016/j.ijheatfluidflow.2020.108737
Received 19 May 2020; Received in revised form 7 October 2020; Accepted 7 October 2020
Available online 26 October 2020
0142-727X/© 2020 The Authors. Published by Elsevier Inc. This is an open access article under the CC BY license (http://creativecommons.org/licenses/by/4.0/).

for simplifying the flow structures and make replication studies easier, but it is not realistic. In contrast, when testing geometries at full scale (Veldhuizen et al., 2016; Grover and Visser, 2006) it is not possible to test as many configurations. The varying yaw angle and turbulence level increase the required sampling time to maintain a given measurement uncertainty, with Tunay et al. (2018) showing that the wake structures and turbulent wake quantities are significantly impacted by crossflow.

Howell et al. (2018) has also shown the importance of encompassing more realistic conditions. Howell et al. (2018) presented several real vehicles, some of which have a very similar drag coefficient at 0° yaw, that had a very different drag response to a crosswind. These cases highlight the importance of considering more realistic conditions in aerodynamic studies.

Several recent studies have investigated the influence of asymmetric drag reduction devices with side wind conditions using tapering (Varney et al., 2018a; Garcia de la Cruz et al., 2017) or pulsed pneumatic jets (Li et al., 2018) on the trailing side edges of the geometry. It is concluded that these devices reduce drag by improving the lateral symmetry in the wake shown in the results from flow field measurements (Li et al., 2018), variance of base pressure gradients (Garcia de la Cruz et al., 2017) or fluctuations of side force (Varney et al., 2018a). If these devices were to be implemented with the correct control strategy then the additional wind averaged drag reductions that could be achieved are approximately 30% for a model without wheels (Garcia de la Cruz et al., 2017; Varney et al., 2018a) and up to 20% for a model with wheels (Varney et al., 2018a).

From this, there is potential for further drag reduction using a combination of an asymmetric roof- and side-tapering. In this work, the tapering angle is allowed to vary along the sides and roof of the geometry, resulting in 9 different small flaps, located at the trailing edge of a rearward-facing tapered cavity. This allows the design space to contain designs similar to previously published geometries (Urquhart et al., 2018; Varney et al., 2018a; Garcia de la Cruz et al., 2017) while allowing for increased flexibility. To investigate this, the flap angles are optimised in the Loughborough University Large Wind Tunnel using a surrogate model based optimisation algorithm. Force measurements, base pressures and full wake Tomographic Particle Image Velocimetry are used to increase the understanding of the drag reduction mechanisms.

2. Methodology

2.1. Test facility

The wind tunnel tests were performed in the Loughborough University Large Wind Tunnel, Fig. 1, which is an open return, closed test section facility. The rectangular working section is 1.92 m × 1.3 m with 0.2 m corner fillets and is 3.6 m long. The tunnel is capable of speeds up to 45 m/s with a freestream turbulence intensity of 0.2% and a flow uniformity of ±0.4% (Johl, 2010).

2.2. Geometry

The geometry used in this study is a modified version of the Windsor body, a generic simplified automotive test case that has been used extensively in the literature to study fundamental flow problems (Volpe et al., 2014; Pavia and Passmore, 2018; Pavia et al., 2018; Perry et al., 2016a; Pavia et al., 2020; Favre and Efraimsson, 2011) and geometry modifications (Perry and Passmore, 2013; Howell et al., 2013; Varney et al., 2018b). The modifications to the Windsor geometry have been applied by Pavia and Passmore (2018), adding wheels to better simulate a real vehicle as shown in Fig. 2a. In this configuration, the body gives a blockage ratio of 4.7% and represents approximately a 25% road vehicle.

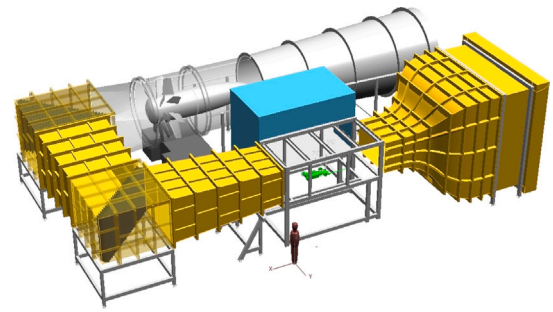

Fig. 1. The Loughborough University Large Wind Tunnel (Johl, 2010).

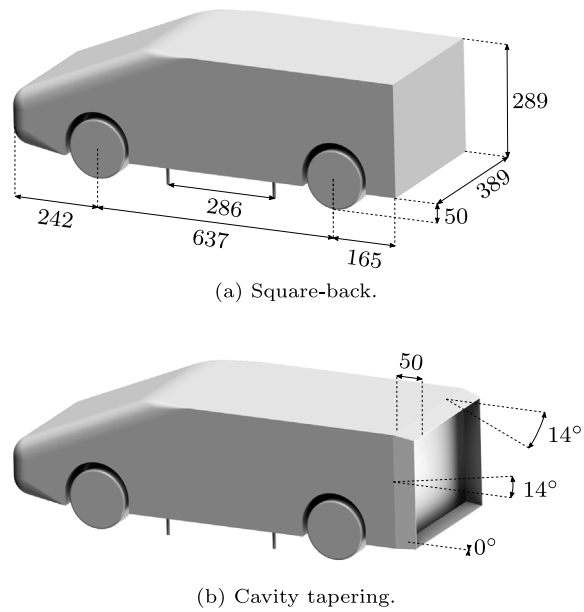

Fig. 2. Windsor geometry with wheels. Measurements are given in mm.

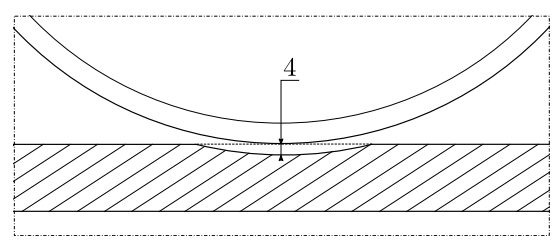

Fig. 3. Debossed floor pad to avoid grounding the model. Measurements are given in mm.

The model is mounted with four 8 mm pins which are located between the wheels to minimise interaction with the overall flow. The wheels are stationary and mounted to the model, with the bottom of the wheels set to be tangential to the tunnel floor. This is achieved without grounding the geometry by using a debossed floor pad, giving a constant 4 mm of clearance between the wheel and the floor, as shown in Fig. 3. The ride height of the geometry is fixed at 50 mm, giving a non-dimensionalised ride height of 0.17 times the base height, with the pitch and roll angle of the geometry set to be 0° ± 0.1°.

The baseline geometry for the optimisation is a 50 mm (5% of the body length) deep cavity with thin (3 mm) walls, with a 14° roof and side edge taper and a 0° diffuser, shown in Fig. 2b. The taper angle for the roof, sides and diffuser were optimised using steady-state CFD simulations with a low $y^+ < 1$ k-ω SST turbulence model. The mesh

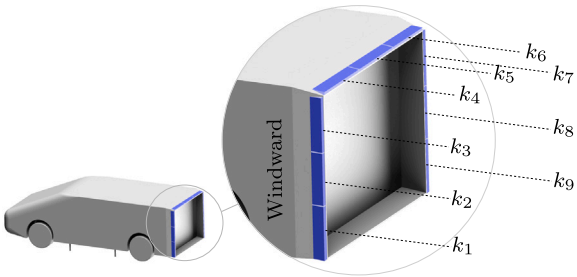

Fig. 4. Naming convention for individual flaps.

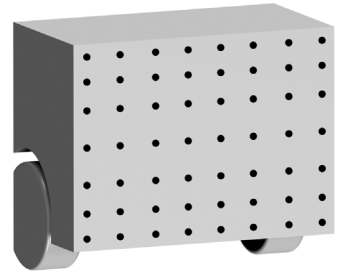

Fig. 5. Distribution of the 7 × 8 wall static pressure measurement locations.

consisted of approximately 90×10^6 hexahedral dominant cells. Each flap design was simulated at 0°, 5° and 10° yaw and the output drag coefficients weighted to form a drive cycle equivalent drag value

$$C_{\mathrm{DWC}} = 0.53C_{\mathrm{D0^\circ\ yaw}} + 0.345C_{\mathrm{D5^\circ\ yaw}} + 0.13C_{\mathrm{D10^\circ\ yaw}}. \tag{1}$$

This is the approach used by Varney et al. (2018a) which omits the 15° yaw term in the original formulation by Howell et al. (2018). The optimised cavity, with 14° side- and roof-edge tapering and a 0° diffuser, is similar to that reported in previous work on cavities in crosswind conditions (Sterken et al., 2014).

The optimisation in this work is applied to small flaps, 20 mm, or 2% of the model length, placed along the sides and roof of the tapered cavity in a similar way to the trailing edge kick by Sterken et al. (2014) and Urquhart et al. (2018). Unlike the previous work, the trailing edge kick is split into three equal flap sections along each edge, totalling nine flaps. These are numbered from 1–9 in a clockwise fashion facing the rear of the vehicle, Fig. 4. The diffuser is not equipped with flaps to simplify the tests.

Due to manufacturing limitations, only positive, outward, flap angles were able to be tested. The flaps were manufactured at four discrete angles, 0°, 7°, 14° and 21°. Each flap has locating pins to ensure correct placement when manually changing them between tests. Based on the works by Varney et al. (2018a) and Garcia de la Cruz et al. (2017) it is expected that negative, inward, flap angles would allow further drag reduction. Increasing the number of flap sections and using continuously variable angles is also expected to improve the maximum achievable drag reduction.

Only negative yaw angles were tested experimentally to avoid obscuring part of the wake from the cameras when performing PIV. Because of this, all these results are mirrored to reflect a positive yaw angle with the nose pointing right following the SAE standard J1594 (0000). In the presented results, the wind moves from left to right in the vehicle driving direction.

2.3. Force measurements

All force and pressure measurements were taken with a freestream velocity, v_∞, of 40 m/s as measured at a pitot-static tube 1.15 m upstream of the model leading edge. This results in a Reynolds number, based on the square root of the frontal area of the vehicle, of $Re_{\mathrm{H}} = 9.4 \times 10^5$. The balance data was sampled at 300 Hz for 300 s with an arithmetic mean taken in post-processing.

All coefficients have been calculated without any blockage correction to allow for direct comparison to computational work. The coefficient calculations are presented in Eqs. (2)–(4), where A is the model's projected frontal area (m^2), ρ is the calculated air density (kg/m^3), v_∞ is the freestream velocity as measured at the pitot tube upstream (m/s) and L_w is the length of the wheelbase. The coefficients are defined as

$$C_{\mathrm{force}} = \frac{Force}{\frac{1}{2}\rho A v_\infty^2} \tag{2}$$

$$C_{\mathrm{moment}} = \frac{Moment}{\frac{1}{2}\rho L_w A v_\infty^2} \tag{3}$$

$$C_{\mathrm{RL}} = \frac{1}{2}C_{\mathrm{L}} - C_{\mathrm{M,Pitch}} \tag{4}$$

where the subscript RL denotes rear lift. The vehicle yaw moment is defined using the right-hand rule along the axis of lift, i.e. a positive yaw moment pulls the vehicle nose left.

The repeatability between tests was estimated by running the same configuration on different days, resulting in a total of 7 unique samples. From these samples, the 95% confidence interval was calculated to ±1 counts at 0° yaw, ±2 at 5° yaw and ±2.5 at 10° yaw, where one count is $\Delta C_{\mathrm{D}} = 0.001$.

2.4. Pressure measurements

The surface static pressure measurements were recorded for 300 s at 260 Hz using a 64 channel differential pressure scanner via 500 mm long smoothbore silicone tubing. The scanner was located inside the model with all necessary cabling existing behind the forward model pins to minimise their impact on the bulk flow.

As the pressure scanner employs a multiplexed analogue to the digital stage, a correction is applied to the data to time-align each of the 64 channels to the first channel for each sample. The implementation of this is well documented by Wood (2015). No additional corrections are applied for the frequency response, as no frequency analysis is to be performed, and no blockage correction is applied to make comparisons with computational work straightforward.

The distribution of pressure tappings on the base is presented in Fig. 5. The pressure coefficient is referenced to a pitot-static tube upstream and using Eq. (5). Where p_t is the total pressure and p_s is the static pressure measured at the pitot-static probe.

$$C_{\mathrm{P}} = \frac{p - p_s}{\frac{1}{2}\rho v_\infty^2} = \frac{p - p_s}{p_t - p_s} \tag{5}$$

To calculate the contribution of the base of the model to the overall drag, the pressure coefficient for each tapping location is integrated using Eq. (6) and by associating an incremental area with each tapping. Using the same analysis as the force measurements, the repeatability was $\pm 0.002C_{\mathrm{DB}}$. The resulting value is representative of the base drag, but as neither the internal and external walls of the cavity are pressure tapped it does not represent the total contribution to the rear pressure drag.

$$C_{\mathrm{DB}} = \frac{1}{A}\int_A C_{\mathrm{P}} \cdot dA \tag{6}$$

2.5. Tomographic particle image velocimetry

The flow field of the near wake has been captured using tomographic Particle Image Velocimetry (PIV), using commercially available hardware and software (DaVis® 8.4) from LaVision®.

For each measurement 1000 image pairs were taken at a frequency of 5 Hz, resulting in 200 s of data. This quantity of samples has been shown by previous authors to be adequate for capturing the bulk wake structure of these, and similar geometries, with tomographic and planar PIV (Pavia et al., 2019, 2020; Perry et al., 2016a).

The volume captured in the tomographic PIV was 550 mm × 480 mm × 380 mm in the x, y and z direction, chosen based on capturing the full width and height of the wake, including some freestream, and the wake closure based on previous work (Pavia et al., 2020; Perry et al., 2016a; Pavia and Passmore, 2018).

To capture the full volume 4 cameras were used in an approximate star configuration as shown in Fig. 6. Two cameras were Imager Pro X 4M cameras (4 MP) and two were sCMOS cameras (5 MP). All the images were reduced to 25% of their original resolution in post-processing to reduce computational expense.

All the cameras were equipped with Nikon® lenses with a 35 mm focal length. To satisfy the Scheimpflug condition the f-stop was set to $f^{\#} = 8$ for all the cameras, as a compromise between depth of field through the volume and allowing enough light to enter the sensor to image the flow field.

The cameras were oriented such that the inclusive angle between them was 60°, resulting in a reconstruction quality of approximately 0.95 (Scarano, 2013).

Initial calibration was performed using a 2D calibration plate located in five positions within the field of view: streamwise centreline, the two streamwise outer edges, and two diagonals. The final calibration was achieved by performing several *self-calibration* iterations. This process results in a map of the position of a region of the image to a region of the volume for each of the cameras, resulting in an RMS error, between a true rectilinear grid and reconstructed one, of less than 0.006 pixels.

The particles used in this experiment are Helium Filled Soap Bubbles (HSFB), using a seeder provided by LaVision®, which are 300 μm in diameter. Large volume tomographic PIV relies on much-reduced light intensity so the seeding medium in this experiment is Helium Filled Soap Bubbles with a diameter of 300 μm. As the reflectance is a cubed relationship with the size of the particle (Adrian and Yao, 1985), allowing the particles to appear brighter with a less power-dense light source. This approach has been used extensively in the literature (Perry et al., 2016a; Caridi et al., 2016; Kühn et al., 2011; Pavia et al., 2019, 2020) and the particles have been shown to follow the flow similarly to other seeding mediums (Scarano et al., 2015)

Three seeding rakes have been used in this experiment, each consisting of 10 nozzles, each of which is capable of producing 40,000 HSFB per second. The seeders are positioned at the start of the working section, shown in Fig. 6b, one horizontally to seed the boundary layer and underbody flow and two to seed the bulk flow. Whilst this will increase the levels of turbulence experienced by the model, it is unavoidable to ensure even seeding of the shear layers. The seeding was continuous throughout the testing due to the open return design of the tunnel resulting in few to no HSFB particles being recirculated.

Illumination of the volume was provided with a 200 mJ Nd:YAG double-pulse laser from Litron®. The laser beam was passed through a volume optic that was chosen to ensure that ≈60% of the peak power from the Gaussian distribution covered the volume of interest. No Fresnel lens or knife-edge optics were used, as at this scale they are prohibitively expensive.

The current setup of the seeder does not produce sufficient bubbles to generate high quality PIV data at 40 m/s, and for this same model, Varney (2020) concluded that the velocity needs to exceed 20 m/s in order to achieve a Reynolds insensitive flow field. Therefore the PIV was conducted at 30 m/s as a compromise between Reynolds sensitivity and maintaining a seeding density of ≈ 0.02 particles per pixel at 25% resolution, to achieve a lower particle reconstruction error (Elsinga et al., 2011; Michaelis et al., 2010). The higher velocity of 40 m/s for the forces is used to improve the accuracy of the force measurements due to the absolute accuracy of the balance. The higher velocity also reduces the time needed for averaging of the forces compared to doing the tests at 30 m/s.

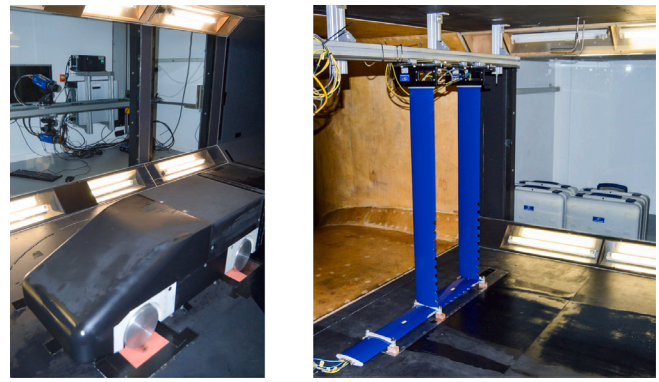

(a) Camera position and orientation relative to the model (b) Seeding set up

Fig. 6. Tomographic set up in the working section.

Table 1
Complete list of PIV processing steps.

Window size (pixels)	Volume binning	Percentage overlap	Number of passes
256	8	75	2
256	4	75	2
128	2	75	2
128	1	75	2
96	1	75	2
64	1	75	2

A series of pre-processing steps were applied to the images to increase the signal to noise ratio between the particles and the background to reduce the reconstruction error. The reconstruction uses the FastMART (Fast Multiplicative Algebraic Reconstruction Technique) as implemented by LaVision® based on the work of Atkinson and Soria (2009). This technique reconstructs the particles in 3D space from a series of 2D images and is performed iteratively, six times, to reduce the number of false-positive reconstructed (*ghost*) particles present in the data (Novara et al., 2010; Scarano, 2013; Elsinga et al., 2006). *Ghost* particles bias the volume to the mean flow of the entire volume (Elsinga et al., 2011), so minimising them is beneficial for data quality.

The vectors were calculated using a direct correlation method with multiple passes. The initial pass used a 256 × 256 × 256 pixel window with a large (× 8) volume bin and ends with a 64 × 64 × 64 pixel window with no volume binning. The intermediate steps are presented in Table 1.

2.6. Optimisation algorithm

Testing all flap angle combinations in the wind tunnel is not possible as there are too many unique combinations, $4^9 = 262\,144$. Instead, the flap angles were optimised for each yaw angle. The optimisation was performed using a surrogate model-based algorithm. Surrogate model-based optimisation algorithms typically perform well when the number of function evaluations is limited, as it is when performing optimisations in a wind tunnel.

The surrogate model was built from an initial design of experiments containing only five samples. The samples were determined using a Latin Hypercube (LHC) where the fifth sample was chosen to be the

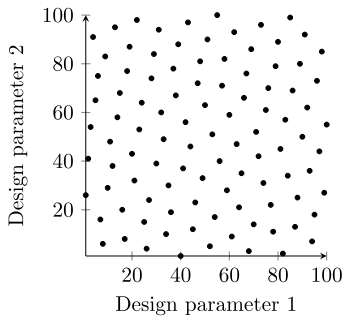

Fig. 7. Latin Hypercube sampling plan containing 100 points.

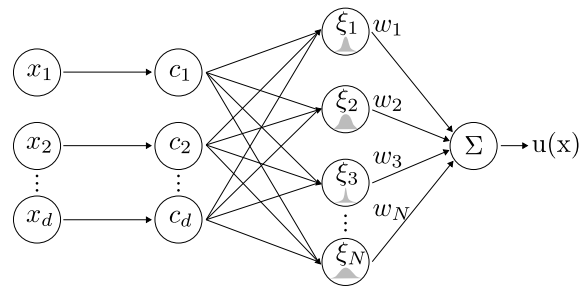

Fig. 8. Radial Basis Function surrogate model network structure.

smooth taper, i.e. all flap angles are set to 0°. The LHC plan divides each design parameter into equally sized intervals where the same value of a parameter can only occur once. The placement of the samples is optimised to increase the separation distance between samples.

The optimisation algorithm for the LHC sampling plan is based on the work by Bates et al. (2004), extended to include categorical, or discrete, design parameters as the tested flaps were only manufactured in 4 discrete angles. An example of an optimised LHC sampling plan containing 100 points for two design dimensions can be seen in Fig. 7.

The surrogate model is based on Radial Basis Function (RBF) interpolation. That is analogous to a one-layer neural network. Radial Basis Function interpolation linearly combines the output of each neuron, or Radial Basis Function, in the hidden layer as

$$u(\mathbf{x}) = \sum_{i=1}^{N} w_i \xi_i(\|\mathbf{x} - \mathbf{x_i}\|_2) \tag{7}$$

where w_i are the weights, ξ_i is the Radial Basis Function, N is the number of sampled designs and $\|\mathbf{x}-\mathbf{x_i}\|_2$ denotes the Euclidean distance between the evaluated design $\mathbf{x}$ and the ith design $\mathbf{x_i}$.

The weights w_i are found by solving the linear system

$$\mathbf{Aw} = \mathbf{u} \tag{8}$$

where $\mathbf{A} = A_{ij} = \xi_i(\|x_i - x_j\|_2)$ and $\mathbf{u} = \mathbf{u}(\mathbf{x_i})$ are the known function values at the sample points. A regression term, λ, is added to the diagonal of $\mathbf{A}$, Eq. (8), which relaxes the requirements of the surrogate model being strictly interpolating. This reduces high-frequency oscillations in the surrogate model when the modelled problem contains noise.

The RBFs, ξ_i, employed were the gaussian, $\xi(r) = e^{-(\varepsilon r)^2}$, inverse quadratic, $\xi(r) = \frac{1}{1+(\varepsilon r)^2}$ and inverse multiquadratic, $\xi(r) = \frac{1}{\sqrt{1+(\varepsilon r)^2}}$ basis functions where ε is the width factor determining the size of the RBF.

Radial Basis Functions can exhibit poor performance when there exists a difference in the scale between the input and output dimensions. Each design parameter is therefore normalised and scaled using a scaling factor c_j. The RBFs are radial using the scaled input parameters which, when scaled back, results in the RBFs being ellipsoidal.

The ridge regression term, λ, widths, ε, Radial Basis Function ξ_i and axis scaling c_j are treated as hyperparameters and optimised to improve the surrogate model's predictive performance. The structure of the RBFs network surrogate model is shown in Fig. 8.

To improve the predictive capability of the model an ensemble of 10 surrogate models was used. The median prediction of the surrogate models was used as the function estimate and the standard deviation as an estimate of the model uncertainty. The tests were alternated between sampling the minimum prediction and the maximum standard deviation in the ensemble of surrogate models to exploit and explore the design space. The entire ensemble of surrogate models was retrained every second sample and the sampling process repeated. The surrogate model performance was good when compared to Random Sample, Differential Evolution, Nelder–Mead and Bayesian Optimisation; performing as well, or better than the other algorithms, on 17 out of 18 optimisation benchmark problems (Urquhart et al., 2020).

2.7. Flap angle optimisation

Since the number of possible designs is finite, each location was sampled in the surrogate model to find the design with the lowest predicted drag value and highest standard deviation in the ensemble of surrogate models at each iteration. The design with the lowest predicted drag, as well as the highest standard deviation in the ensemble, was tested before rebuilding the surrogate model with the new information from the tested designs and run again. This was done to both exploit the model prediction and reduce the model uncertainty to explore the design space.

The optimisation was run separately for 0°, 5° and 10° yaw, with the objective to reduce drag. Although sensing of the wind direction was not considered in this work, this replicates the ability of the geometry to adapt to the surrounding wind conditions. A potential method for improving the speed of the optimisation would be to include the yaw angle as a design parameter. This would allow for the low drag information to be *shared* across the design space, but in this instance, it would reduce the opportunities to test the robustness of the optimisation algorithm. At 0° yaw a symmetry constraint was also imposed, i.e. $k_1 = k_9$, $k_2 = k_8$, $k_3 = k_7$, $k_4 = k_6$.

The optimisation was performed for a constrained search range first where each side of the geometry takes on the same flap angle, reducing the number of design parameters from 9 to 3. Once the optimisation was finished in the constrained space, the information was added to the full design space. For the yawed optimisation, five additional LHC sample points were added to cover more of the large design space.

It was not feasible to test all possible designs in a given time frame so the global optimality of the best design tested cannot be guaranteed. The optimisation routine was stopped for each yaw angle when it was expected that no further improvements could be found in close vicinity of the designs already tested. This was done due to a finite amount of available testing time and the assumption that drag is expected to be smooth locally in relation to flap angle changes.

The best flap angles found at each yaw angle will be referred to as the optimised flaps.

The sampling plan was created with the package LatinHypercubeSampling.jl (Urquhart, 2019a) and the surrogate model optimisation using SurrogateModelOptim.jl (Urquhart, 2019b). More information on the sampling plan and the optimisation algorithm can be found in Urquhart et al. (2020).

3. Results & discussion

Results are first presented for zero yaw and then with yaw. At yaw, it is primarily the results at 5° yaw which are discussed.

3.1. 0° yaw

A total of 26 different designs were tested in the wind tunnel at 0° yaw. The optimisation history of these tests can be seen in Fig. 9.

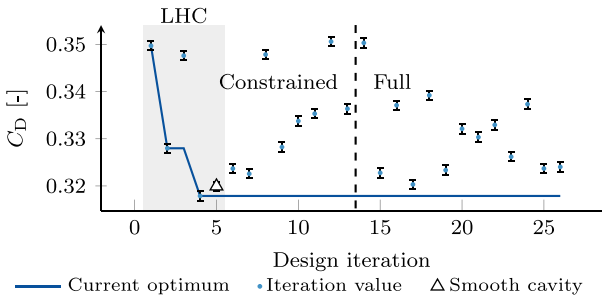

Fig. 9. Flap optimisation history at 0° yaw. Error bars indicate the 95% confidence interval.

Table 2
Aerodynamic force coefficients at 0° yaw.

Configuration.	C_D	C_{FL}	C_{RL}	C_{DB}
Square-back	0.389	0.142	0.002	0.291
Smooth taper	0.320	0.121	0.166	0.200
Optimised flaps	0.318	0.125	0.121	0.201

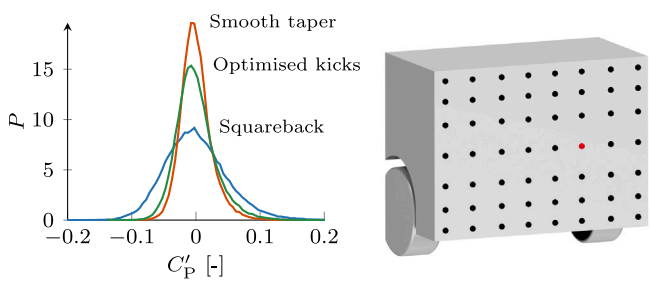

Fig. 10. Probability Density Function (PDF) of the pressure tap for the square-back, smooth taper and optimised flaps configurations.

The force coefficients for the square-back, smooth taper (no flaps) and the best flap angles found are given in Table 2. An improvement of 2 drag counts was found at 0° yaw with 7° flap angles for all the roof positions, design iteration 4.

The tapered cavity, without flaps, adds a significant amount of lift, $0.143\,C_L$ (100%) increase over the square-back, which can impact vehicle high-speed stability (Howell and Le Good, 1999). However, using the optimised flaps, this is brought down to a $0.102\,C_L$ (71%) increase in total lift compared to the square-back. The negative effects of the increased lift could be mitigated by actively adapting the roof flap angles depending on vehicle speed, to keep the lift force below a desired threshold while optimising for drag.

The geometries were investigated for lateral bi-stability as this has previously been reported in the literature for similar geometries (Pavia and Passmore, 2018; Pavia et al., 2018; Perry et al., 2016a; Grandemange et al., 2012, 2013a), and is linked to the vehicle drag. Fig. 10 shows the probability density function for the square-back, smooth taper and optimised flaps configurations on one of the pressure taps located off the centreline where any lateral bi-stable behaviour would be evident.

Bonnavion et al. (2019) also identified vertical wake instabilities for geometries similar to the one investigated here. To identify the vertical position, the pressure gradient, defined as

$$g_z = \frac{1}{2}\left[\frac{C_{P,\,A} - C_{P,\,C}}{z_A - z_C} + \frac{C_{P,\,B} - C_{P,\,D}}{z_B - z_D}\right] \tag{9}$$

is investigated, Fig. 11. There are no signs of vertical or lateral bi-stability for any of the configurations investigated. However, the vertical instability reported by Bonnavion et al. (2019) is sensitive to the pitch angle of the vehicle which can lock the wake into one of the up-

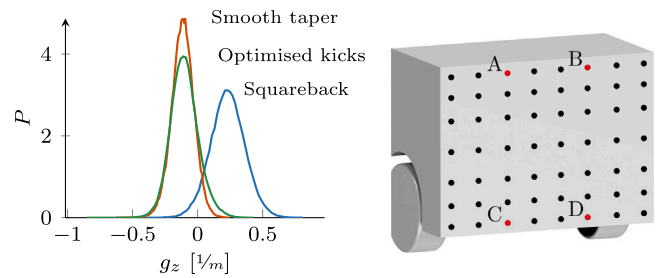

Fig. 11. Probability Density Function (PDF) of the base pressure gradient for the square-back, smooth taper and optimised flaps configurations.

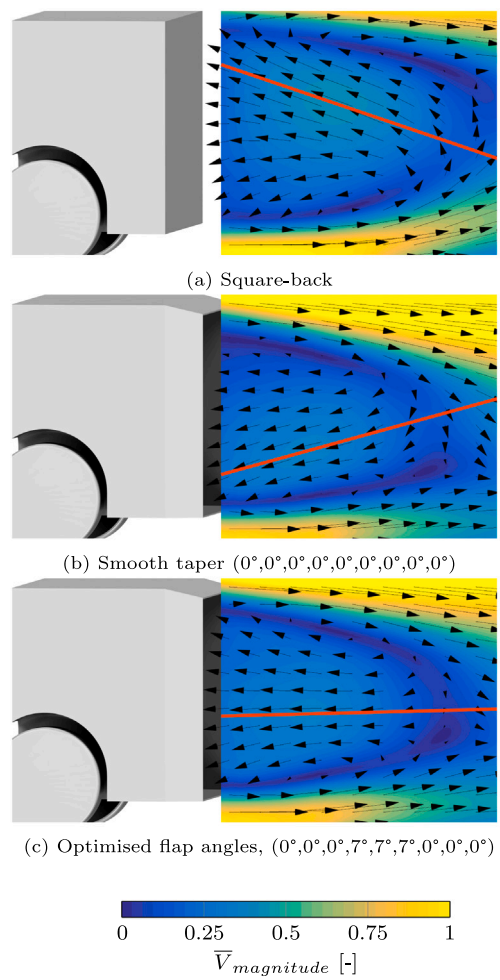

Fig. 12. Centreline velocity magnitude normalised by the freestream velocity. The line is a qualitative addition to indicate the return flow direction.

or down-wash dominated states. Therefore the presence of the vertical wake instability cannot be confirmed or denied in this work as the pitch angle of the model was kept constant. The same analysis was performed for the configurations at yaw yielding similar results.

Fig. 12 shows the centreline velocity magnitude for the square-back, smooth taper and optimised flaps configurations. The flow in the wake is directed more perpendicular to the vehicle base for the design with optimised flaps compared to the smooth taper. This improvement in the wake balance has been linked to improvements in vehicle drag (Urquhart et al., 2018; Wang et al., 2020; Perry, 2016; Varney et al., 2020).

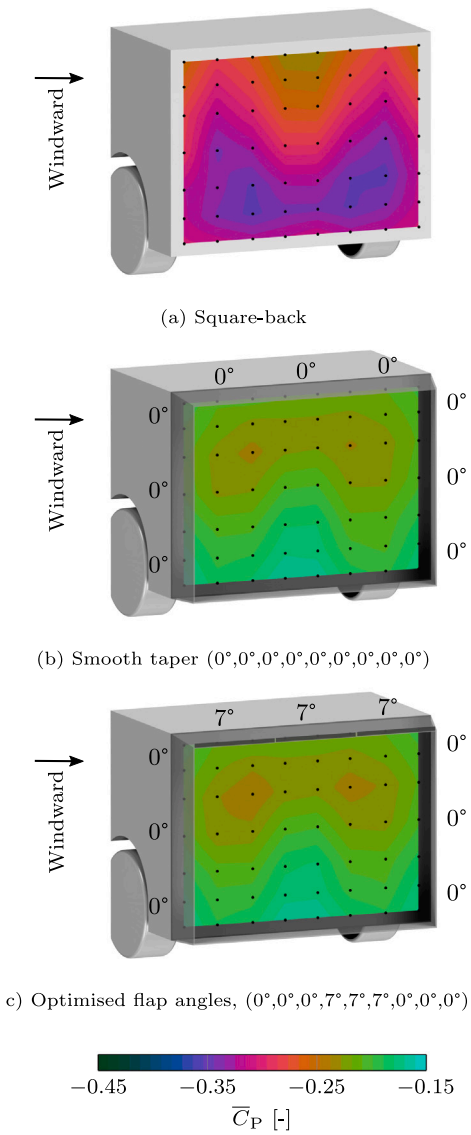

Fig. 13. Base pressure at 0° yaw of the square-back, smooth taper and optimised flap angles. The pressure tap locations are marked in black.

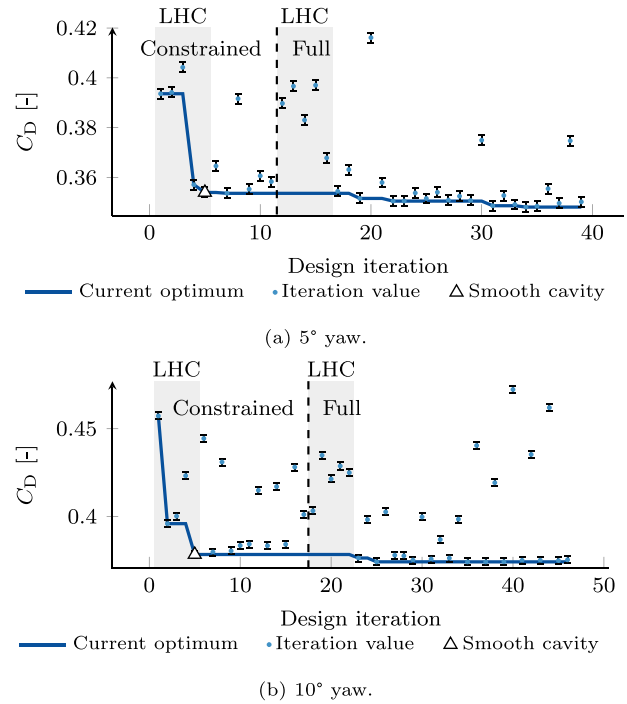

Fig. 14. Flap optimisation history at yaw. Error bars indicate the 95% confidence interval.

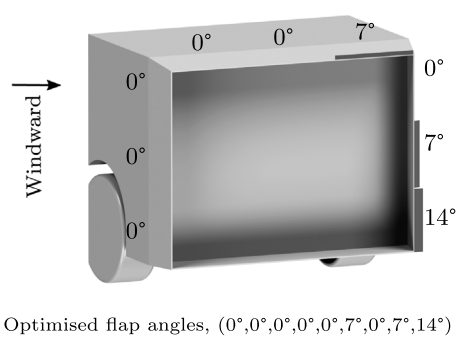

Fig. 15. Windsor geometry with optimised flap angles for 5° and 10° yaw.

The base pressure distributions for these configurations can be seen in Fig. 13. The base pressures are slightly lower for the optimised flaps configuration compared to the smooth taper and the integrated base drag in Table 2 confirms this. Due to the base drag being higher for the optimised flap angles, compared to the smooth taper, it is theorised that the reduction in drag is primarily due to an increase in pressure on the outside of the cavity. When adding the 7° flaps to the roof, the attached flow along the roof is deflected less, resulting in a lower acceleration of the flow and an increase in pressure compared to the smooth taper. This pressure increase outweighs the increase in base drag resulting from the larger wake. The base pressure distribution is similar between the smooth taper and the optimised flaps. This is an unexpected result based on the centreline flow, Fig. 12. It is believed that the flow of the smooth taper and the optimised flaps become more similar closer to the base. Due to the experimental setup this cannot be verified. On a more extreme configuration with 14° flaps on the roof was also tested and this configuration indicated the expected upwash dominated base pressure distribution, not shown here.

3.2. 5° & 10° yaw

Fig. 14 contains the optimisation history of the yawed cases where 39 design were tested at 5° yaw and 46 at 10° yaw. No improvement in drag could be found in the constrained design space for either yaw angle. It was expected that an improvement could only be found in the constrained design space with a 7° or 14° outward flap angle in positions 7–9, with the rest being 0° based on the works by Varney et al. (2018a) and Garcia de la Cruz et al. (2017). None of these configurations improved drag outside of the reported confidence intervals. It was only possible to find a significant improvement over the smooth taper in the full design space.

For both yaw angles, the best design found featured the flap angles 0°,0°,0°,0°,0°,7°,0°,7°,14°, shown in Fig. 15. Each design with a significant drag reduction featured changes towards the leeward side of the model, flap positions 6–9. Several designs have similar improvements to drag, but common to all designs with an improvement of 4 drag counts or more is a non-zero flap on the roof's leeward side, position 6. This was not expected and will be further explored in this section.

The force coefficients for the square-back, smooth taper and the optimised design are given in Table 3.

Table 3
Aerodynamic force coefficients at yaw.

Configuration	C_D	C_{FL}	C_{RL}	C_{DB}	C_{Yaw}
5° yaw					
Square-back	0.435	0.171	0.008	0.322	−0.082
Smooth taper	0.354	0.151	0.183	0.226	−0.124
Optimised flaps	0.348	0.150	0.183	0.223	−0.133
10° yaw					
Square-back	0.482	0.252	0.032	0.357	−0.160
Smooth taper	0.378	0.269	0.242	0.256	−0.209
Optimised flaps	0.374	0.270	0.240	0.254	−0.218

An improvement of 6 drag counts was found for the optimised flap angles over the smooth taper at 5° yaw with a smaller improvement of 4 counts at 10° yaw. Using Eq. (1) to calculate the driving cycle equivalent drag value, the square-back, smooth taper and optimised flaps have 0.419, 0.341 and 0.337 C_{DWC} respectively. In total, a 20% reduction in the cycle average drag is achieved using the optimised flaps over the square-back.

Similar to the 0° yaw situation, the tapered cavity increases total lift significantly, and the differences between the smooth taper and the optimised flaps are negligible. There is, however, a difference in the yaw moment, which increases in magnitude for the optimised flaps. The magnitude in yaw moment is larger for both the smooth taper and optimised flaps, compared to the square-back. This yaw moment response could have a negative effect on vehicle handling as the vehicle yaw rate in gusts has been identified as an indicator of high-speed stability by Brandt et al. (2020). As was suggested for 0° yaw, the negative effects can be omitted by optimising the flap angle depending on the vehicle speed to reduce drag while keeping the aerodynamics forces and moments in relation to vehicle dynamics within defined limits.

Grandemange et al. (2013b) noted a quadratic relationship between drag and lift when investigating a simplified blunt road vehicle with two angled flaps mounted at the top and bottom edge of the base. Fig. 16 shows the relationship between drag and lift for the configurations tested during the optimisation. While drag tends to reduce with increased lift, the spread in drag, for similar lift values, is significant. The same analysis was performed at 0°-yaw showing even larger spread. Table 3 shows a trend between an increase in the absolute yaw moment and a reduction in drag. This is further investigated in Fig. 17. Similarly to lift there is an observable trend, however, the spread in drag is again significant for a similar yaw moment. The remaining forces and moments were investigated as well as $C_L^2+C_S^2$ used by Howell (2015), all showing significant spreads in drag. The large spread in drag is likely due to the complexity of designs which can be achieved using the 9 separate flaps. Using the balance measurements is not enough to explain the changes in drag. It is possible that a quantitative indicator of wake balance would better explain the changes in drag; however, the available flow field data from this study alone is not enough to determine this.

The optimised flap angles reduce the lateral pressure gradient at the base, resulting in a more uniform pressure distribution, Fig. 18. On the windward side of the geometry, the pressure is reduced when adding the optimised flaps. The majority of the drag reduction is due to the increased pressure on the leeward side of the geometry. The base pressure distribution is qualitatively similar between the smooth taper and square-back geometries with low-pressure zones concentrated to the leeward side of the model.

Fig. 19 shows the in-plane velocity magnitude 75 mm, or 7% of the vehicle length, behind the base of the vehicle body (cavity not included). The strength of the rotating structure near the top leeward corner of the base is reduced when using the optimised flap angles, Fig. 19b compared to Figs. 19a and 19c. The small reduction in the strength of this vortex reduces the crossflow within the wake. This can

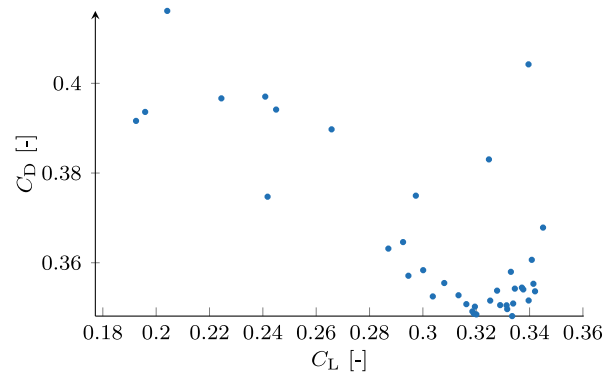

Fig. 16. Coefficient of lift and drag at 5° yaw for all the tested flap angles.

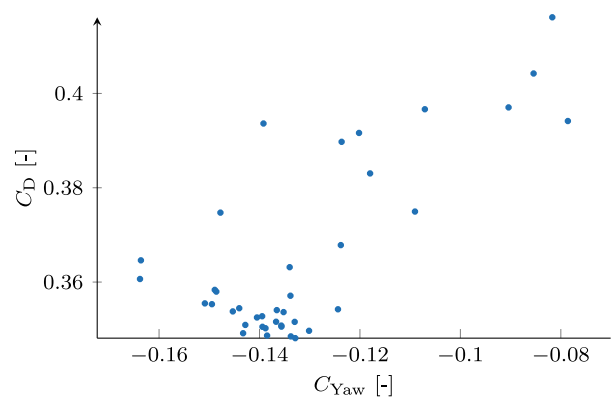

Fig. 17. Coefficient of yaw and drag at 5° yaw for all the tested flap angles.

be seen around the vortex in the top windward corner as well as in the lower leeward portion of the wake in the same figure. The upwash in the windward side of the wake is also reduced by the optimised flaps. This is also observed in the base pressures where the top windward corner of the optimised flaps has a slightly reduced high pressure area, Fig. 18b, compared to the smooth taper Fig. 18c.

The design with optimised flap angles but without the roof flap, $k_6 = 0°$, was also investigated since all configurations with a significant drag reduction featured a non-zero flap angle in that position, Fig. 19c. For this sub-optimal configuration, the wake is pushed outward, similarly to the optimised design. However, the crossflow in the wake is qualitatively more similar to the smooth taper. The 7° flap in position 6 reduces the strength of the top leeward vortex which reduces the crossflow in the entire wake.

The reduction in crossflow in the lower portion of the wake can be seen in Fig. 20 where a top-view of the wake at 1/3 of the base height is shown. The flow impingement is closer to being perpendicular with the optimised flap angles, Fig. 20c, compared to the other configurations.

The sensitivity to flap angles at the optimised design was investigated using the surrogate model and the designs tested during the optimisation. Each flap angle was changed one at a time while keeping the other angles at the optimised values, in Fig. 21. Some configurations were explicitly tested and are indicated by a triangle, the others are estimated using the surrogate model. It is only the explicitly tested configurations which are marked; however, there are several combinations of flaps that are similar but feature more than one changed variable and are not shown.

The flap angle sensitivity analysis suggests that flap positions k_{1-5} could benefit from negative flap angles due to the positive gradient when increasing the flap angle. This is consistent with the results presented by Varney et al. (2018a) and Garcia de la Cruz et al. (2017).

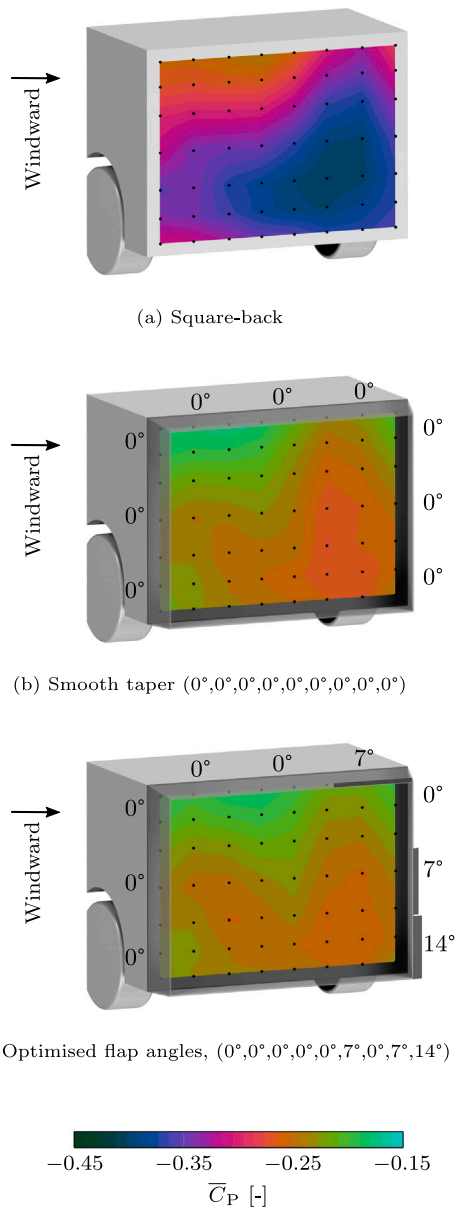

(a) Square-back

(b) Smooth taper (0°,0°,0°,0°,0°,0°,0°,0°,0°)

(c) Optimised flap angles, (0°,0°,0°,0°,0°,7°,0°,7°,14°)

Fig. 18. Base pressure at 5° yaw of the square-back, smooth taper and optimised flap angles. The pressure tap locations are marked in black.

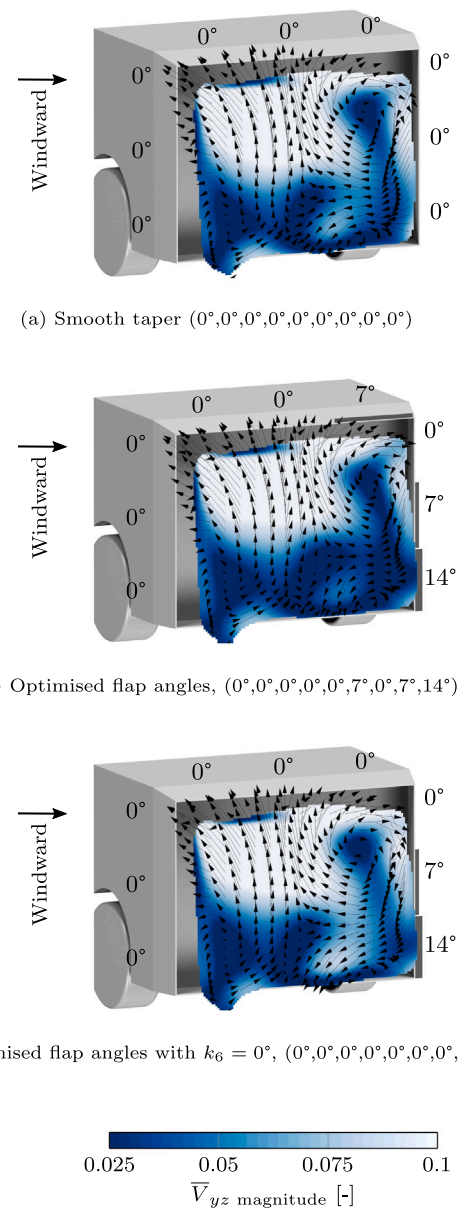

(a) Smooth taper (0°,0°,0°,0°,0°,0°,0°,0°,0°)

(b) Optimised flap angles, (0°,0°,0°,0°,0°,7°,0°,7°,14°)

c) Optimised flap angles with $k_6 = 0°$, (0°,0°,0°,0°,0°,0°,0°,7°,14°)

Fig. 19. In-plane velocity magnitude 75 mm behind the cavity of the smooth taper and optimised flap angles. The values are normalised by the freestream velocity. The plane is clipped where the longitudinal velocity is larger than 25% of the freestream velocity.

Based on the crossflow analysis, Fig. 19, negative flap angles in positions k_{1-5} could reduce the crossflow within the wake. We can also see that flap number 7 carries a drag penalty when increasing the angle above 0°. It is believed that at 0° the strength of the top windward vortex is increased.

The base pressure fluctuations, Fig. 22, indicate a slight increase in unsteadiness for the optimised flap angles over the smooth taper and the bulk wake turbulent kinetic energy follows the same trend, Fig. 23. Higher levels of unsteadiness in the wake shear layers have been associated with increased entrainment of high energy flow into the wake reducing the wake length and increasing drag (Barros et al., 2016; Wang et al., 2019). Grandemange (2013) showed that reducing the spanwise turbulent fluctuations across a mixing layer increases the pressure on the low velocity side. Reducing the spanwise turbulent fluctuations for a bluffbody would reduce drag, if all else is equal. Han et al. (2013) applied unsteady flow control to a simplified vehicle model which reduced the shear layer instabilities, elongating the wake and reducing drag. However, Perry et al. (2016b) and Evrard et al. (2016) have separately shown on a bi-stable geometry that a global increase in wake unsteadiness, measured as the time between switches between the bi-stable states, correlates well with reduced aerodynamic drag.

The overall increased levels of unsteadiness for the optimised flap angles coupled with the drag reduction indicate that the improvement to drag is primarily due to an improved wake balance. I.e. the flow is impinging the base with an angle that is closer to being perpendicular.

In Fig. 24 the Q-criterion is used to identify the vortical structures in the wake. Both the leeward and the windward vortices along the top of the geometry can be identified in both configurations and are largely unaffected by the optimised flap angles. The largest change between the geometries is to the size and strength of the rotating structure in the top leeward corner of the base which is consistent with the crossflow analysis.

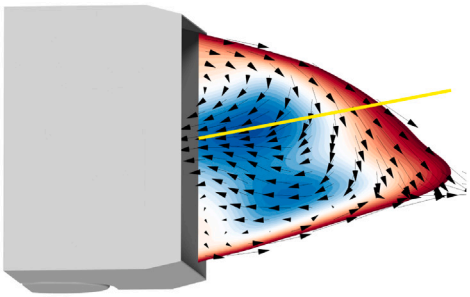

(a) Smooth taper, (0°,0°,0°,0°,0°,0°,0°,0°,0°)

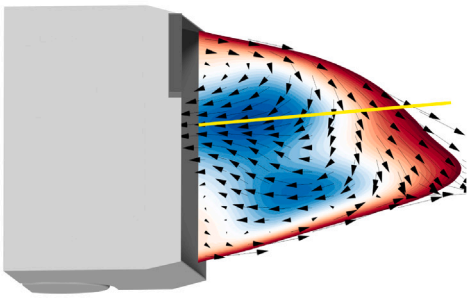

(b) Optimised flap angles, (0°,0°,0°,0°,0°,7°,0°,7°,14°)

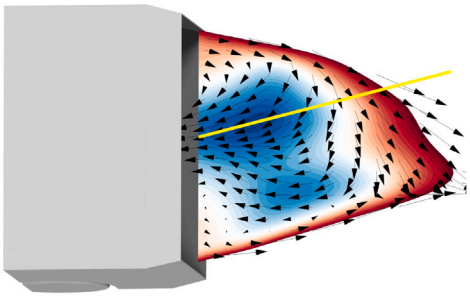

(c) Optimised flap angles with $k_6 = 0°$, (0°,0°,0°,0°,0°,0°,0°,7°,14°)

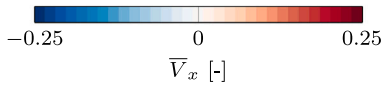

Fig. 20. Longitudinal velocity at 1/3 of the base height for the smooth taper and optimised flap angles. The values are normalised by the freestream velocity. The line is a qualitative addition to indicate the return flow direction. The plane is clipped where the longitudinal velocity is larger than 25% of the freestream velocity.

The time-averaged aerodynamic drag can also be calculated by applying the momentum equation,

$$\overline{C_D}A = \int_S \left[-\overline{C_P} - 2\left(\frac{\overline{v_x^2}}{\overline{v_\infty^2}} - \frac{\overline{v_x}}{\overline{v_\infty}} \right) \right] dS \tag{10}$$

to a sufficiently large control volume (Fourrié et al., 0000). The viscous terms have been dropped as they are orders of magnitude smaller than the other terms. To reduce drag, the loss in pressure and longitudinal velocity need to be reduced over the integrated area. In this work, wake plane pressures were not measured and the area captured by the PIV measurements is not large enough to accurately calculate the drag coefficient.

Instead, the crossflow and longitudinal velocities within the wake are integrated as

$$\overline{C_{\text{crossflow}}}A = \int_{S_{\text{wake}}} \left[\frac{\sqrt{\overline{v_y}^2 + \overline{v_z}^2}}{\overline{v_\infty}} \right] dS_{\text{wake}} \tag{11}$$

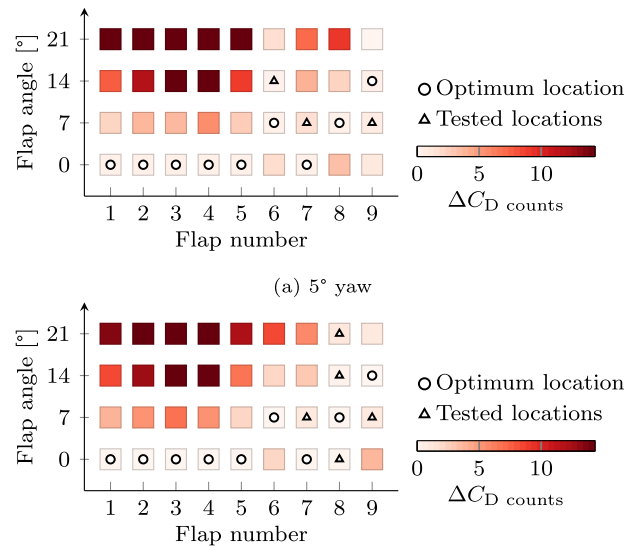

Fig. 21. Sensitivity to flap angle changes of each flap, while keeping the other flap angles constant at the best found design. Tested design locations only include designs which were explicitly tested.

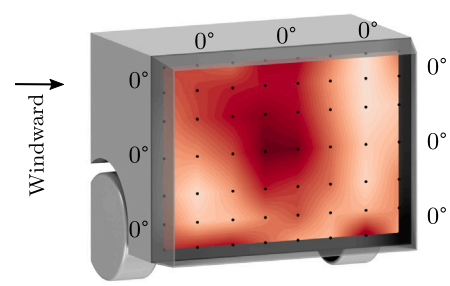

(a) Smooth taper (0°,0°,0°,0°,0°,0°,0°,0°,0°)

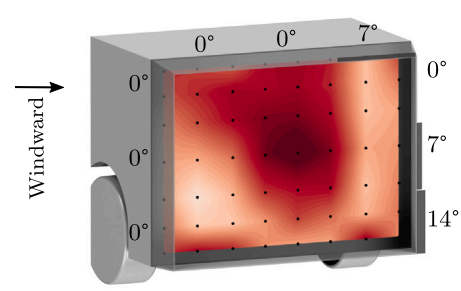

(b) Optimised flap angles (0°,0°,0°,0°,0°,7°,0°,7°,14°)

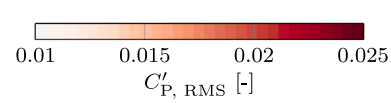

Fig. 22. Base pressure fluctuations at 5° yaw of the smooth taper and optimised flap angles. The pressure tap locations are marked in black.

and

$$\overline{C_{\text{longitudinal}}}A = \int_{S_{\text{wake}}} \left[\frac{\overline{v_x}}{\overline{v_\infty}} \right] dS_{\text{wake}} \tag{12}$$

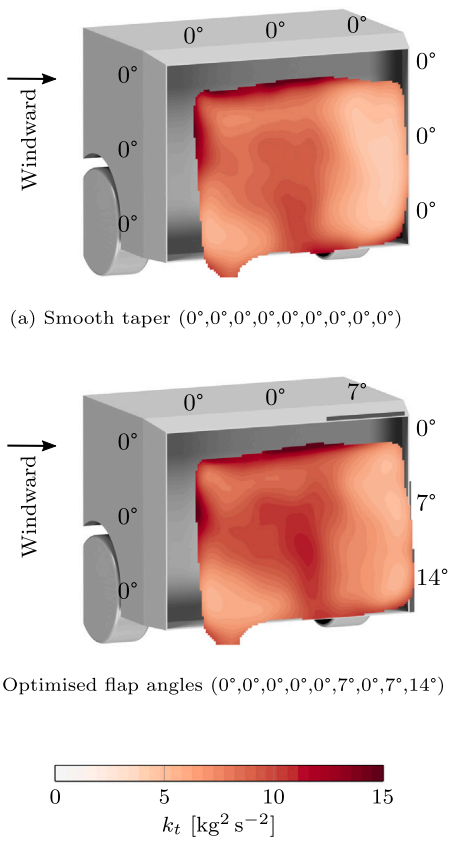

(a) Smooth taper (0°,0°,0°,0°,0°,0°,0°,0°,0°)

(b) Optimised flap angles (0°,0°,0°,0°,0°,7°,0°,7°,14°)

Fig. 23. Time averaged turbulent kinetic energy 50 mm behind the cavity at 5° yaw of the smooth taper and optimised flap angles. The plane is clipped where the longitudinal velocity is larger than 25% of the freestream velocity.

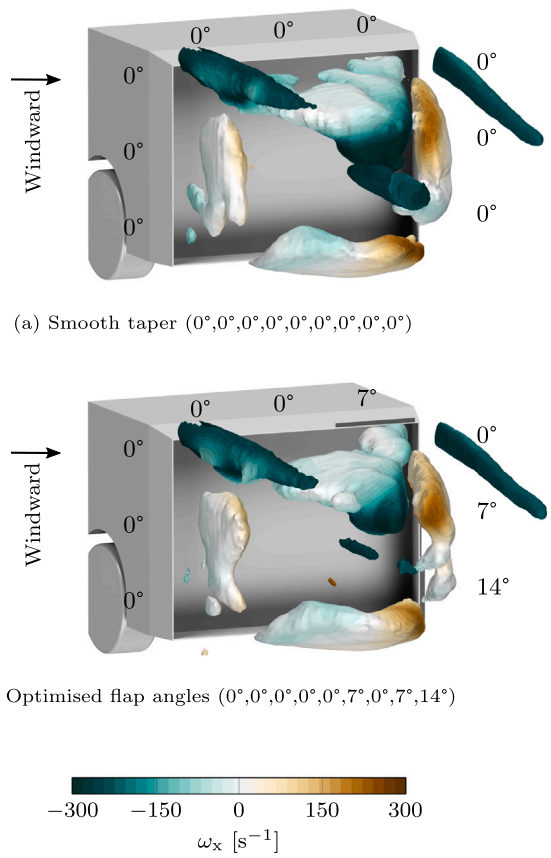

(a) Smooth taper (0°,0°,0°,0°,0°,0°,0°,0°,0°)

(b) Optimised flap angles (0°,0°,0°,0°,0°,7°,0°,7°,14°)

Fig. 24. ISO surface of $Q_{\text{criterion}}$ at 10 000 s^{-2} for 5° yaw of the smooth taper and optimised flap angles. Negative vorticity indicate structures rotating clockwise in the figure.

respectively. The wake surface, S_{wake}, is defined as the region where the longitudinal velocity, $\overline{V_x}$, is smaller than $0.25V_\infty$.

The crossflow cannot be directly related to drag quantitatively, instead, it is used here to investigate the previously presented qualitative results, and are shown in Fig. 25.

The optimised flap angles reduce the crossflow within the wake while increasing the longitudinal velocity towards the base, compared to the smooth taper.

The combination of low crossflow and larger negative longitudinal velocities within the wake is prevalent for the low drag configurations and is consistent with other work (Urquhart et al., 2018; Perry, 2016). The same analysis was performed for the 0° yaw configurations, showing similar trends. This could be used as a qualitative indicator to improve vehicle design in relation to drag.

4. Concluding remarks

In this work, a simplified model with nine flaps, located at the trailing edge of a rearward-facing tapered cavity, was tested in a wind tunnel. The angles of the flaps were optimised using a surrogate model-based algorithm. The optimised geometry features a positive flap angle on the leeward roof side which reduces the strength of a large scale rotating structure in the wake. This results in a 2% decrease in drag at yaw compared to the tapered cavity without flaps. The positive roof flap was an unexpected result based on the available literature and would not have been found without the use of an optimisation algorithm.

Analysis of the flow field using tomographic PIV and base pressures suggest that it is mainly an improvement to the wake balance which resulted in a reduction in drag. The analysis also suggests that further drag reduction could be achieved by using inward angles on the flaps located at the windward side. The wake unsteadiness and base pressure fluctuations alone could not be linked to changes in drag.

The integration of crossflow within the wake confirms that the optimised flap angles reduce the crossflow within the vehicle wake. This was accompanied by an increase in the longitudinal velocity towards the base. The crossflow within the wake is a useful qualitative indicator of drag which could be used in vehicle design.

CRediT authorship contribution statement

Magnus Urquhart: Conceptualization, Formal analysis, Investigation, Methodology, Software, Visualization, Writing - original draft, Writing - review & editing. **Max Varney:** Conceptualization, Formal analysis, Investigation, Methodology, Visualization, Writing - original draft, Writing - review & editing. **Simone Sebben:** Project administration, Resources, Supervision, Writing - review & editing. **Martin Passmore:** Project administration, Resources, Supervision, Writing - review & editing.

Declaration of competing interest

The authors declare that they have no known competing financial interests or personal relationships that could have appeared to influence the work reported in this paper.

Acknowledgements

The authors would like to thank Matthew Ward for all the help and assistance during the wind tunnel tests. The authors would also like

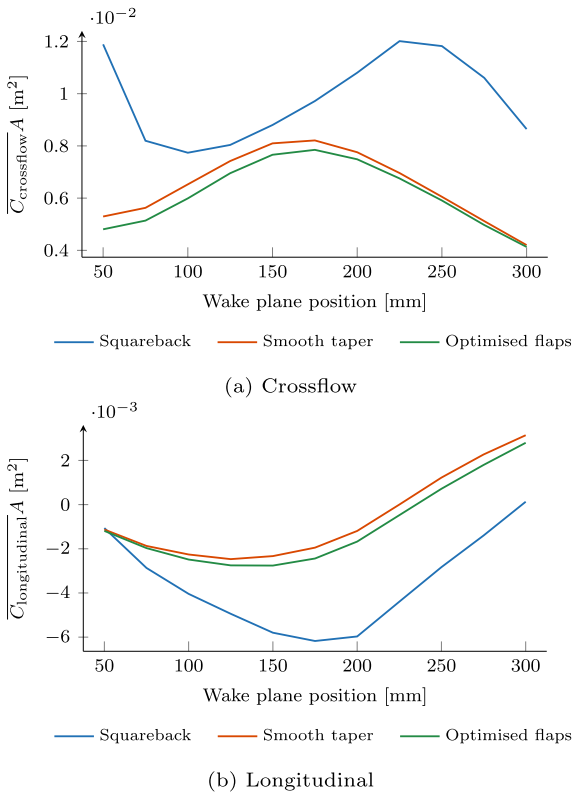

Fig. 25. Integrated longitudinal and crossflow velocities within the wake. Wake plane distance is referenced relative to the base of the vehicle body (cavity not included). The integration planes used are placed every 25 mm.

to thank Alexander Broniewicz and Lennert Sterken from the Volvo Car Corporation for their valuable input and support throughout the project. The simulations were performed on resources provided by the Swedish National Infrastructure for Computing (SNIC) at NSC (SNIC, 2019).

Funding

This work is funded by the Swedish Energy Agency grant number P43328-1.

References

Adrian, R., Yao, C.S., 1985. Pulsed laser technique application to liquid and gaseous flows and the scattering power of seed materials. Appl. Opt. 24 (1), 44–52.

Ahmed, S.R., Ramm, G., Faltin, G., 1984. Some salient features of the time-averaged ground vehicle wake. In: SAE Tech. Pap. 840300. SAE International, http://dx.doi.org/10.4271/840300.

Atkinson, C., Soria, J., 2009. An efficient simultaneous reconstruction technique for tomographic particle image velocimetry. Exp. Fluids 47 (4–5), 553.

Barros, D., Borée, J., Noack, B.R., Spohn, A., Ruiz, T., 2016. Bluff body drag manipulation using pulsed jets and Coanda effect. J. Fluid Mech. 805, 422–459. http://dx.doi.org/10.1017/jfm.2016.508, URL: https://www.cambridge.org/core/journals/journal-of-fluid-mechanics/article/bluff-body-drag-manipulation-using-pulsed-jets-and-coanda-effect/12609816D2FF77F5372BA9B3E32F69A8.

Bates, S., Sienz, J., Toropov, V., 2004. Formulation of the optimal latin hypercube design of experiments using a permutation genetic algorithm. 2011. http://dx.doi.org/10.2514/6.2004-2011.

Bonnavion, G., Cadot, O., 2018. Unstable wake dynamics of rectangular flat-backed bluff bodies with inclination and ground proximity. J. Fluid Mech. 854, 196–232. http://dx.doi.org/10.1017/jfm.2018.630, URL: https://www.cambridge.org/core/product/identifier/S0022112018006304/type/journal_article.

Bonnavion, G., Cadot, O., Herbert, V., Parpais, S., Vigneron, R., Délery, J., 2019. Asymmetry and global instability of real minivans' wake. J. Wind Eng. Ind. Aerodyn. 184, 77–89. http://dx.doi.org/10.1016/j.jweia.2018.11.006, URL: https://linkinghub.elsevier.com/retrieve/pii/S0167610518307578.

Brandt, A., Sebben, S., Jacobson, B., Preihs, E., Johansson, I., 2020. Quantitative High Speed Stability Assessment of a Sports Utility Vehicle and Classification of Wind Gust Profiles. pp. 2020–01–0677. http://dx.doi.org/10.4271/2020-01-0677, URL: https://www.sae.org/content/2020-01-0677/.

Caridi, G.C.A., Ragni, D., Sciacchitano, A., Scarano, F., 2016. HFSB-seeding for large-scale tomographic PIV in wind tunnels. Exp. Fluids 57 (12), 1–13. http://dx.doi.org/10.1007/s00348-016-2277-7.

Cooper, K.R., 1985. The effect of front-edge rounding and rear-edge shaping on the aerodynamic drag of bluff vehicles in ground proximity. In: SAE Int. Congr. Expo.. SAE International, http://dx.doi.org/10.4271/850288.

Garcia de la Cruz, J.M., Brackston, R.D., Morrison, J.F., 2017. Adaptive Base-Flaps Under Variable Cross-Wind. http://dx.doi.org/10.4271/2017-01-7000, URL: http://www.sae.org/content/2017-01-7000/.

Duell, E.G., George, a.R., 1993. Measurements in the unsteady near wakes of ground vehicle bodies. In: SAE Tech. Pap.. SAE International, http://dx.doi.org/10.4271/930298, URL: http://www.sae.org/technical/papers/930298.

Elsinga, G.E., Scarano, F., Wieneke, B., van Oudheusden, B.W., 2006. Tomographic particle image velocimetry. Exp. Fluids 41 (6), 933–947. http://dx.doi.org/10.1007/s00348-006-0212-z.

Elsinga, G.E., Westerweel, J., Scarano, F., Novara, M., 2011. On the velocity of ghost particles and the bias errors in Tomographic-PIV. Exp. Fluids 50 (4), 825–838. http://dx.doi.org/10.1007/s00348-010-0930-0.

European Parliament, Council of the European Union, 2014. Regulation (EU) no 333/2014 of the european parliament and of the council of 11 march 2014 amending regulation (EC) no 443/2009 to define the modalities for reaching the 2020 target to reduce CO 2 emissions from new passenger cars the. Off. J. Eur. Union 15–21.

Evrard, A., Cadot, O., Herbert, V., Ricot, D., Vigneron, R., Délery, J., 2016. Fluid force and symmetry breaking modes of a 3D bluff body with a base cavity. J. Fluids Struct. 61, 99–114. http://dx.doi.org/10.1016/j.jfluidstructs.2015.12.001, URL: https://linkinghub.elsevier.com/retrieve/pii/S0889974615002698.

Favre, T., Efraimsson, G., 2011. An assessment of detached-eddy simulations of unsteady crosswind aerodynamics of road vehicles. Flow Turbul. Combust. 87 (1), 133–163. http://dx.doi.org/10.1007/s10494-011-9333-4.

Fourrié, G., Keirsbulck, L., Labraga, L., Gilliéron, P., Bluff-body drag reduction using a deflector. 50 (2) 385–395. http://dx.doi.org/10.1007/s00348-010-0937-6. URL: http://link.springer.com/10.1007/s00348-010-0937-6.

Grandemange, M., 2013. Analysis and Control of Three-dimensional Turbulent Wakes: from Axisymmetric Bodies to Road Vehicles (Ph.D. thesis). ENSTA Paris, p. 238.

Grandemange, M., Cadot, O., Gohlke, M., 2012. Reflectional symmetry breaking of the separated flow over three-dimensional bluff bodies. Phys. Rev. E 86 (3), 035302. http://dx.doi.org/10.1103/PhysRevE.86.035302, URL: https://link.aps.org/doi/10.1103/PhysRevE.86.035302.

Grandemange, M., Gohlke, M., Cadot, O., 2013a. Bi-stability in the turbulent wake past parallelepiped bodies with various aspect ratios and wall effects. Phys. Fluids 25 (9), 095103. http://dx.doi.org/10.1063/1.4820372, URL: http://aip.scitation.org/doi/10.1063/1.4820372.

Grandemange, M., Mary, A., Gohlke, M., Cadot, O., 2013b. Effect on drag of the flow orientation at the base separation of a simplified blunt road vehicle. Exp. Fluids 54 (5), 1529. http://dx.doi.org/10.1007/s00348-013-1529-z, URL: http://link.springer.com/10.1007/s00348-013-1529-z.

Grover, K., Visser, K.D., 2006. Over-the-road tests of sealed aft cavities on tractor trailers. In: SAE Tech. Pap.. SAE International, http://dx.doi.org/10.4271/2006-01-3529.

Han, X., Krajnović, S., Basara, B., 2013. Study of active flow control for a simplified vehicle model using the PANS method. Int. J. Heat Fluid Flow 42, 139–150. http://dx.doi.org/10.1016/j.ijheatfluidflow.2013.02.001, URL: https://linkinghub.elsevier.com/retrieve/pii/S0142727X13000337.

Howell, J., 2015. Aerodynamic drag of passenger cars at yaw. SAE Int. J. Passeng. Cars - Mech. Syst. 8 (1), http://dx.doi.org/10.4271/2015-01-1559, URL: http://papers.sae.org/2015-01-1559/.

Howell, J., Le Good, G., 1999. The Influence of Aerodynamic Lift on High Speed Stability. pp. 1999–01–0651. http://dx.doi.org/10.4271/1999-01-0651, URL: https://www.sae.org/content/1999-01-0651/.

Howell, J., Passmore, M., Tuplin, S., 2013. Aerodynamic drag reduction on a simple car-like shape with rear upper body taper. SAE Int. J. Passeng. Cars - Mech. Syst. 6, 52–60. http://dx.doi.org/10.4271/2013-01-0462.

Howell, J., Passmore, M., Windsor, S., 2018. A drag coefficient for test cycle application. SAE Int. J. Passeng. Cars - Mech. Syst. 11 (5), 447–461. http://dx.doi.org/10.4271/2018-01-0742, URL: https://www.sae.org/content/2018-01-0742/.

J1594. Vehicle Aerodynamics Terminology (J1594 Ground Vehicle Standard) - SAE Mobilus. URL: https://saemobilus.sae.org/content/j1594_199412.

JATO, 2019. Demand for SUVs slows to lowest recorded rate in june, indicating that registrations may have peaked in the European market. URL: https://www.jato.com/demand-for-suvs-slows-to-lowest-recorded-rate-in-june-indicating-that-registrations-may-have-peaked-in-the-european-market/.

Johl, G., 2010. The Design and Performance of a 1.9m x 1.3m Indraft Wind Tunnel (Ph.D. thesis). Loughborough University.

Kühn, M., Ehrenfried, K., Bosbach, J., Wagner, C., 2011. Large-scale tomographic particle image velocimetry using helium-filled soap bubbles. Exp. Fluids 50 (4), 929–948. http://dx.doi.org/10.1007/s00348-010-0947-4.

Li, R., Borée, J., Noack, B.R., Cordier, L., Harambat, F., 2018. Drag Reduction of a Yawed Car Model by Combining Fluidic Flaps and Turbulence Control. p. Presentation Only.

Michaelis, D., Novara, M., Scarano, F., Wieneke, B., 2010. Comparison of volume reconstruction techniques at different particle densities. In: 15th Int Symp Appl. Laser Tech. to Fluid Mech. Lisbon, Port.. pp. 5–8.

Novara, M., Batenburg, K.J., Scarano, F., 2010. Motion tracking-enhanced MART for tomographic PIV. Meas. Sci. Technol. 21 (3), 35401. http://dx.doi.org/10.1088/0957-0233/21/3/035401, URL: http://stacks.iop.org/0957-0233/21/i=3/a=035401?key=crossref.0ec58c90e4b5153ada11adcbded0c100.

Pavia, G., Passmore, M., 2018. Characterisation of wake bi-stability for a square-back geometry with rotating wheels. In: Wiedemann, J. (Ed.), Prog. Veh. Aerodyn. Therm. Manag.. Springer International Publishing, Cham, pp. 93–109.

Pavia, G., Passmore, M., Sardu, C., 2018. Evolution of the bi-stable wake of a square-back automotive shape. Exp. Fluids 59 (1), 1–20. http://dx.doi.org/10.1007/s00348-017-2473-0.

Pavia, G., Passmore, M.A., Varney, M., Hodgson, G., 2020. Salient three-dimensional features of the turbulent wake of a simplified square-back vehicle. J. Fluid Mech. 888, A33. http://dx.doi.org/10.1017/jfm.2020.71.

Pavia, G., Varney, M., Passmore, M., Almond, M., 2019. Three dimensional structure of the unsteady wake of an axisymmetric body. Phys. Fluids 31 (2), 025113. http://dx.doi.org/10.1063/1.5078379, URL: http://aip.scitation.org/doi/10.1063/1.5078379.

Perry, A.K., 2016. An Investigation into the Base Pressure of Simplified Automotive Squareback Geometries. Loughborough University, URL: https://dspace.lboro.ac.uk/2134/22605.

Perry, A.K., Almond, M., Passmore, M.a., Littlewood, R., 2016a. The study of a bi-stable wake region of a generic squareback vehicle using tomographic PIV. In: SAE World Congr.. http://dx.doi.org/10.4271/2016-01-1610.

Perry, A.K., Passmore, M., 2013. The impact of underbody roughness on rear wake structure of a squareback vehicle. In: SAE Tech. Pap. 2013-01-0463. SAE International, http://dx.doi.org/10.4271/2013-01-0463.

Perry, A.-K., Pavia, G., Passmore, M., 2016b. Influence of short rear end tapers on the wake of a simplified square-back vehicle: wake topology and rear drag. 57 (11) 169. http://dx.doi.org/10.1007/s00348-016-2260-3. URL: http://link.springer.com/article/10.1007/s00348-016-2260-3.

Scarano, F., 2013. Tomographic PIV: principles and practice. Meas. Sci. Technol. 24 (1), 12001. http://dx.doi.org/10.1088/0957-0233/24/1/012001, URL: http://stacks.iop.org/0957-0233/24/i=1/a=012001.

Scarano, F., Ghaemi, S., Caridi, G.C.A., Bosbach, J., Dierksheide, U., Sciacchitano, A., 2015. On the use of helium-filled soap bubbles for large-scale tomographic PIV in wind tunnel experiments. Exp. Fluids 56 (2), 42. http://dx.doi.org/10.1007/s00348-015-1909-7.

Schuetz, T., 2015. Aerodynamics of road vehicles, fifth edition. SAE International, http://dx.doi.org/10.4271/r-430.

SNIC, 2019. Swedish national infrastrucutre for computing. URL: http://www.snic.se/.

Sterken, L., Löfdahl, L., Sebben, S., Walker, T., 2014. Effect of rear-end extensions on the aerodynamic forces of an SUV. In: SAE Technical Papers. http://dx.doi.org/10.4271/2014-01-0602, URL: http://papers.sae.org/2014-01-0602/.

Tunay, T., Firat, E., Sahin, B., 2018. Experimental investigation of the flow around a simplified ground vehicle under effects of the steady crosswind. Int. J. Heat Fluid Flow 71, 137–152. http://dx.doi.org/10.1016/j.ijheatfluidflow.2018.03.020, URL: https://linkinghub.elsevier.com/retrieve/pii/S0142727X17308706.

Urquhart, M., 2019a. Latinhypercubesampling.jl - release v1.4.0. https://github.com/MrUrq/LatinHypercubeSampling.jl.

Urquhart, M., 2019b. Surrogatemodeloptim.jl - release v0.4.1. https://github.com/MrUrq/SurrogateModelOptim.jl.

Urquhart, M., Ljungskog, E., Sebben, S., 2020. Surrogate-based optimisation using adaptively scaled radial basis functions. Appl. Soft Comput. 88, http://dx.doi.org/10.1016/j.asoc.2019.106050.

Urquhart, M., Sebben, S., Sterken, L., 2018. Numerical analysis of a vehicle wake with tapered rear extensions under yaw conditions. J. Wind Eng. Ind. Aerodyn. 179, 308–318. http://dx.doi.org/10.1016/j.jweia.2018.06.001, URL: https://www.sciencedirect.com/science/article/pii/S0167610518301144.

Varney, M., 2020. Base Drag Reduction for Squareback Road Vehicles (thesis). Loughborough University, http://dx.doi.org/10.26174/thesis.lboro.11823759.v1, URL: https://repository.lboro.ac.uk/articles/Base_drag_reduction_for_squareback_road_vehicles/11823759.

Varney, M., Passmore, M., Gaylard, A., 2018a. Parametric study of asymmetric side tapering in constant cross wind conditions. SAE Int. J. Passeng. Cars - Mech. Syst. 11 (3), 213–224. http://dx.doi.org/10.4271/2018-01-0718, URL: http://www.sae.org/content/2018-01-0718/.

Varney, M., Passmore, M., Gaylard, A., 2018b. Parametric study of asymmetric side tapering in constant cross wind conditions.

Varney, M., Passmore, M., Swakeen, R., Gaylard, A., 2020. Parametric Study of Reduced Span Side Tapering on a Simplified Model with Wheels. pp. 2020–01–0680. http://dx.doi.org/10.4271/2020-01-0680, URL: https://www.sae.org/content/2020-01-0680/.

Veldhuizen, R., van dr Krieke, J.P., Van Raemodnck, G.M.R., 2016. Design of a Rear-End Aerodynamic Drag Reduction Device for Semi-Trailers. Technical Report, Institution of Mechanical Engineers, London, pp. 89–100.

Volpe, R., Ferrand, V., Da Silva, A., Le Moyne, L., 2014. Forces and flow structures evolution on a car body in a sudden crosswind. J. Wind Eng. Ind. Aerodyn. 128, 114–125. http://dx.doi.org/10.1016/j.jweia.2014.03.006, URL: http://linkinghub.elsevier.com/retrieve/pii/S0167610514000506.

Wang, Y., Sicot, C., Borée, J., Grandemange, M., 2020. Experimental study of wheel-vehicle aerodynamic interactions. J. Wind Eng. Ind. Aerodyn. 198, 104062. http://dx.doi.org/10.1016/j.jweia.2019.104062, URL: http://www.sciencedirect.com/science/article/pii/S0167610519306622.

Wang, B., Yang, Z., Zhu, H., 2019. Active flow control on the 25° Ahmed body using a new unsteady jet. Int. J. Heat Fluid Flow 79, 108459. http://dx.doi.org/10.1016/j.ijheatfluidflow.2019.108459, URL: https://linkinghub.elsevier.com/retrieve/pii/S0142727X18310270.

Wood, D., 2015. The Effect of Rear Geometry Changes on the Notchback Flow Field (Ph.D. thesis). Loughborough University.